Highlights

- Neural trajectories in the hippocampus exhibited greater variability during a working memory (WM) task compared to those in the entorhinal cortex and amygdala regions.

- The distance of neural trajectories between encoding and retrieval states in the hippocampus was memory-load dependent during a WM task.

- Hippocampal neural trajectories fluctuated between the encoding and retrieval states in a task-dependent manner during both baseline and sharp-wave ripple (SWR) periods.

- Hippocampal neural trajectories shifted from encoding to retrieval states during SWR period.

Hippocampal Neural Fluctuations Between Memory Encoding and Retrieval States During a Working Memory Task in Humans

Yusuke Watanabe[a,*], Yuji Ikegaya[b,c,d], Takufumi Yanagisawa[a,e]

[a]*Institute for Advanced Cocreation studies, Osaka University, 2-2 Yamadaoka, Suita, 565-0871, Osaka, Japan*
[b]*Graduate School of Pharmaceutical Sciences, The University of Tokyo, 7-3-1 Hongo, Tokyo, 113-0033, Japan*
[c]*Institute for AI and Beyond, The University of Tokyo, 7-3-1 Hongo, Tokyo, 113-0033, Japan*
[d]*Center for Information and Neural Networks, National Institute of Information and Communications Technology, 1-4 Yamadaoka, Suita City, 565-0871, Osaka, Japan*
[e]*Department of Neurosurgery, Osaka University Graduate School of Medicine, 2-2 Yamadaoka, Osaka, 565-0871, Japan*

Abstract

Working memory (WM) is crucial for a multitude of cognitive functions, but its underlying neural mechanisms at play remain to be fully understood. Interestingly, the hippocampus and sharp-wave ripples (SWRs)— transient and synchronous oscillation observed in the hippocampus — garner recognition for their significance in memory consolidation and retrieval, albeit their correlation with WM tasks remains to be elucidated. Here we show that during a WM task, multi-unit activity patterns in the hippocampus display distinctive dynamics, especially during SWR periods. This study analyzed intracranial electroencephalography data from the medial temporal lobe (MTL) of nine patients with epilepsy, recorded during an eight-second Sternberg task. Utilizing Gaussian-process factor analysis, we extracted low-dimensional neural representations or trajectories (NT) within MTL regions during the Sternberg WM task. The results revealed significant variations in NT of the hippocampus compared to those of the entorhinal cortex and the amygdala. Additionally, the distance of the NT between the encoding and retrieval phases was dependent on memory load. Crucially, hippocampal NT oscillated during the retrieval phase between encoding and retrieval states in a task-dependent manner. Notably, these fluctuations shifted from encoding to retrieval states during SWR episodes. These findings reaffirm the role of the hippocampus in WM tasks and propose a hypothesis: the hippocampus transitions its functional state from encoding to retrieval during SWRs in WM tasks.

Keywords: working memory, memory load, hippocampus, sharp-wave ripples, humans

7 figures, 3 tables, 221 words for abstract, and 3114 words for main text

1. Introduction

Working memory (WM) is crucial in everyday life; however, its neural mechanism has yet to be fully elucidated. Specifically, the hippocampus's involvement in WM processing, a pivotal region for memory, is the subject of ongoing research [1] [2] [3] [4] [5] [6] [7] [8] [9]. Understanding the hippocampus' role in working memory is instrumental in deepening our comprehension of cognitive processes and could potentially enhance cognitive abilities.

Current evidence suggests that a transient, synchronized oscillation, called sharp-wave ripples (SWRs) [10], is associated with several cognitive functions. These include memory replay [11] [12] [13] [14] [15], memory consolidation [16] [17] [18] [19], memory recall [20] [21] [22], and neural plasticity [23] [24]. These associations suggest that SWR may be a fundamental computational manifestation of hippocampal processing, contributing to working memory performance as well.

Recent studies have found that low-dimensional representations in hippocampal neurons can explain WM task performances. Specifically, the firing patterns of

*Corresponding author. Tel: +81-6-6879-3652 Email: ywatanabe@alumni.u-tokyo.ac.jp

place cells [25] [26] [27] [28] [29], found in the hippocampus, have been identified within dynamic, non-linear three-dimensional hyperbolic spaces in rats [30]. Additionally, grid cells in the entorhinal cortex (EC), which is the main pathway to the hippocampus [31] [32] [33], exhibited a toroidal geometry during exploration in rats [34].

However, these studies primarily focus on spatial navigation in rodents, which poses limitations. To illustrate, the temporal resolution of navigation tasks is inadequate as the timing of memory acquisition and recall is not clearly delineated. Consequently, there is a relative paucity of research on the impact of SWRs on WM performance [35]. Further, the presence of noise in signals recorded during rodent movement complicates the detection of SWRs [36]. Therefore, to clarify the relationship between SWRs and WM tasks, research with human subjects is necessary.

Considering these factors, this study investigates the hypothesis that hippocampal neurons exhibit unique neural trajectories (NTs) in low-dimensional space, particularly during SWR periods, in response to WM tasks in humans. To test this hypothesis, we employed a dataset of patients performing an eight-second Sternberg task (1 s for fixation, 2 s for encoding, 3 s for maintenance, and 2 s for retrieval) with high temporal resolution. Intracranial electroencephalography (iEEG) signals within the medial temporal lobe (MTL) were recorded for these patients [37]. To investigate low-dimensional NTs, we utilized Gaussian-process factor analysis (GPFA), an established method for analyzing neural population dynamics [38].

2. Methods

2.1. Dataset

The dataset used in this study, which is publicly available, comprises nine epilepsy patients performing a modified the Sternberg task [37]. This task includes four phases: fixation (1s), encoding (2s), maintenance (3s), and retrieval (2s). During the encoding phase, participants were presented with a set of four, six, or eight alphabet letters. They were then tasked with determining whether a probe letter displayed during the retrieval phase had previously appeared (the correct response for Match IN task) or not (the correct response for Mismatch OUT task). Intracranial electroencephalography (iEEG) signals were captured with a 32 kHz sampling rate within a 0.5–5,000 Hz frequency range, using depth electrodes in the MTL regions: the anterior head of the left and right hippocampus (AHL and AHR), the posterior body of the hippocampus (PHL and PHR), the entorhinal cortex (ECL and ECR), and the amygdala (AL and AR), as depicted in Figure 1A and Table 1. The iEEG signals were subsequently downsampled to 2 kHz. Correlations between variables such as set size and correct rate were examined (Figure ??S1). Multiunit spike timing was determined via a spike sorting algorithm [39] using the Combinato package (`https://github.com/jniediek/combinato`)(Figure 1C).

2.2. Calculation of NT using GPFA

NTs, also referred to as 'factors', in the hippocampus, EC, and amygdala were determined using GPFA [38] applied to the multi-unit activity data for each session, performed with the elephant package (`https://elephant.readthedocs.io/en/latest/reference/gpfa.html`). The bin size was set to 50 ms, without overlaps. Each factor was z-normalized across all sessions, and the Euclidean distance from the origin (O) was then computed.

For each NT within a region such as AHL, geometric medians (g_F for fixation, g_E for encoding, g_M for maintenance, and g_R for retrieval phase) were calculated by determining the median coordinates of the NT during the four phases. An optimal GPFA dimensionality was found to be three using the elbow method obtained by examining the log-likelihood values through a three-fold cross-validation approach (Figure 2B).

2.3. Identifying SWR candidates from hippocampal regions

Potential SWR events within the hippocampus were detected using a widely used method [40]. LFP signals from a region of interest (ROI) like AHL, were re-referenced by deducting the averaged signal from locations outside the ROI (for instance, AHR, PHL, PHR, ECL, ECR, AL, and AR). The re-referenced LFP signals were then filtered with a ripple-band filter (80–140 Hz) to determine SWR candidates, marked as SWR$^+$ candidates. SWR detection was carried out using a published tool (`https://github.com/Eden-Kramer-Lab/ripple_detection`) [41], with the bandpass range adjusted to 80–140 Hz for humans

[21] [22], unlike the initial 150–250 Hz range typically applied to rodents.

Control events for SWR⁺ candidates, labeled as SWR⁻ candidates, were detected by randomly shuffling the timestamps of SWR⁺ candidates across all trials and subjects. The resulting SWR⁺/SWR⁻ candidates were then visually inspected.

2.4. Defining SWRs from putative hippocampal CA1 regions

Potential SWRs were differentiated from SWR candidates in putative CA1 (cornu Ammonis 1) regions. These regions were initially defined as follows: SWR⁺/SWR⁻ candidates in the hippocampus were projected into a two-dimensional space based on overlapping spike counts per unit using a supervised method, UMAP (Uniform Manifold Approximation and Projection) [42]. Clustering validation was performed by calculating the silhouette score [43] from clustered samples. Regions in the hippocampus, which scored above 0.6 on average across sessions (75th percentile), were identified as putative CA1 regions, resulting in the identification of five electrode positions from five patients.

SWR⁺/SWR⁻ candidates in these predetermined CA1 regions were categorized as SWR⁺/SWR⁻, and thus they no longer retained their candidate status. The duration and ripple band peak amplitude of SWRs were found to follow log-normal distributions. Each time period of SWR was partitioned relative to the time from the SWR center into pre- (at −800 ms to −300 ms from the SWR center), mid- (at −250 to +250 ms), and post-SWR (at +300 to +800 ms) times.

2.5. Statistical Evaluation

Both the Brunner–Munzel test and the Kruskal-Wallis test were executed using the SciPy package in Python [44]. Correlational analysis was conducted by determining the rank of the observed correlation coefficient within its associated set-size-shuffled surrogate using a customized Python script. The bootstrap test was implemented with an in-house Python script.

3. Results

3.1. iEEG Recording and NT in MTL Regions during the Sternberg Task

Our analysis employed a publicly accessible dataset [37], which comprises LFP signals (Figure 1A) from MTL regions (Table 1) recorded during the execution of the modified Sternberg task. We extracted SWR⁺ candidates from LFP signals that were filtered in the 80–140 Hz ripple band (Figure 1B), originating in all hippocampal regions (refer to Methods section). Meanwhile, SWR⁻ candidates, control events for SWR⁺ candidates, were defined at the same timestamps but distributed across different trials (Figure 1). The dataset encompassed multi-unit spikes (Figure 1C), recognized via a spike sorting algorithm [39]. Employing GPFA [38], we applied this to 50-ms windows of binned multi-unit activity without overlaps to determine the NTs, or factors, of MTL regions by session and region (Figure 1D). We normalized each factor per session and region, for instance, session #2 in AHL of subject #1. We then calculated the Euclidean distance from the origin (O) (Figure 1E).

3.2. Correlation of Hippocampal NT with the Sternberg Task

Figure 2A exhibits a distribution of median NTs, comprising 50 trials, within the three main factor spaces. Utilizing the elbow method, we established the optimal embedding dimension for the GPFA model as three (Figure 2B). The NT distance from the origin (O) — represented as $\|g_F\|$, $\|g_E\|$, $\|g_M\|$, and $\|g_R\|$ — in the hippocampus surpassed the corresponding distances in the EC and amygdala (Figure 2C & D).[1]

Similarly, we computed the distances between the geometric medians of four phases, namely $\|g_F g_E\|$, $\|g_F g_M\|$, $\|g_F g_R\|$, $\|g_E g_M\|$, $\|g_E g_R\|$, and $\|g_M g_R\|$. The hippocampus showed larger distances between phases than those in the EC and amygdala.[2]

---

[1]Hippocampus: Distance = 1.11 [1.01], median [IQR], n = 195,681 timepoints; EC: Distance = 0.94 [1.10], median [IQR], n = 133,761 timepoints; Amygdala: Distance = 0.78 [0.88], median [IQR], n = 165,281 timepoints.

[2]Hippocampus: Distance = 0.60 [0.70], median [IQR], n = 8,772 combinations; EC: Distance = 0.28 [0.52], median [IQR], n = 5,017 combinations ($p < 0.01$; Brunner–Munzel test); Amygdala: Distance = 0.24 [0.42], median [IQR], n = 7,466 combinations ($p < 0.01$; Brunner–Munzel test).

3.3. Memory-Load-Dependent NT Distance between Encoding and Retrieval States in the Hippocampus

Regarding memory load in the Sternberg task, we observed a negative correlation between the correct rate of trials and the set size, which denotes the number of letters to be encoded (Figure 3A).[3] Concomitantly, a positive correlation was noted between the response time and set size (Figure 3B).[4].

Next, we discovered a positive correlation between set size and the NT distance separating the encoding and retrieval phases ($\log_{10}\|g_Eg_R\|$) (Figure 3C).[5]. However, distances between other phase combinations did not highlight statistically significant correlations (Figures 3D and **??**).

3.4. Detection of Hippocampal SWRs from Putative CA1 Regions

To enhance the precision of recording sites and SWR detection, we approximated the electrode placements in the CA1 regions of the hippocampus using distinguished multi-unit spike patterns during SWR events. SWR$^+$/SWR$^-$ candidates from each session and hippocampal region were embedded in two-dimensional space using UMAP (Figure 4A).[6] With the silhouette score as a quality metric for clustering (Figure 4B and Table 2), recording sites demonstrating an average silhouette score exceeding 0.6 across all sessions were identified as putative CA1 regions.[7] (Tables 2 and 3). We identified five putative CA1 regions, four of which were not indicated as seizure onset zones (Table 1).

Subsequently, SWR$^+$/SWR$^-$ candidates within these putative CA1 regions were labeled as SWR$^+$ and SWR$^-$, respectively[8] (Table 3). Both SWR$^+$ and SWR$^-$ manifested identical durations [9] due to their definitions and followed a log-normal distribution (Figure 4C). During the initial 400 ms of the retrieval phase, an increase in SWR$^+$ incidence was found[10] (Figure 4D). The peak ripple band amplitude of SWR$^+$ surpassed that of SWR$^-$ and followed a log-normal distribution (Figure 4E).[11].

3.5. Transient Change in Hippocampal NT during SWR

We assessed the 'distance' of the NT from the origin (O) during SWR events in both encoding and retrieval phases (Figure 5A). Observing the increase in distance during SWR, as illustrated in Figure 5A, we categorized each SWR into three stages: pre-, mid-, and post-SWR. Hence, the distances from the origin O during those SWR intervals are identified as $\|\text{pre-eSWR}^+\|$, $\|\text{mid-eSWR}^+\|$ and others.

As a result, $\|\text{mid-eSWR}^+\|$[12] exceeded $\|\text{pre-eSWR}^+\|$[13], and $\|\text{mid-rSWR}^+\|$[14] was larger than $\|\text{pre-rSWR}^+\|$ in both the Match IN and Mismatch OUT tasks.[15]

3.6. Visualization of Hippocampal NT during SWR in Two-Dimensional Spaces

Having observed NT 'jumping' during SWR (Figure 5), we visualized the three-dimensional NTs of pre-, mid-, and post-SWR events during the encoding and retrieval phases (Figure 6). The distance between these was found to be memory-load dependent (Figure 3).

---

[3]Correct rate: set size four (0.99 ±0.11, mean ±SD; n = 333 trials) vs. set size six (0.93 ±0.26; n = 278 trials; $p < 0.001$, Brunner–Munzel test with Bonferroni correction) and set size eight (0.87 ±0.34; n = 275 trials; $p < 0.05$; Brunner–Munzel test with Bonferroni correction). Generally, $p < 0.001$ for Kruskal–Wallis test; correlation coefficient = - 0.20, $p < 0.001$.

[4]Response time: set size four (1.26 ±0.45 s; n = 333 trials) vs. set size six (1.53 ±0.91 s; n = 278 trials) and set size eight (1.66 ±0.80 s; n = 275 trials). All comparisons $p < 0.001$, Brunner–Munzel test with Bonferroni correction; $p < 0.001$ for Kruskal–Wallis test; correlation coefficient = 0.22, $p < 0.001$

[5]Correlation between set size and $\log_{10}(\|g_Eg_R\|)$: correlation coefficient = 0.05, $p < 0.001$. Specific values: $\|g_Eg_R\|$ = 0.54 [0.70] for set size four, n = 447; $\|g_Eg_R\|$ = 0.58 [0.66] for set size six, n = 381; $\|g_Eg_R\|$ = 0.61 [0.63] for set size eight, n = 395.

[6]Consider the AHL in session #1 of subject #1 as a case in point.

[7]The identified regions were the AHL of subject #1, AHR of subject #3, PHL of subject #4, AHL of subject #6, and AHR of subject #9.

[8]These definitions produced equal counts for both categories: SWR$^+$ (n = 1,170) and SWR$^-$ (n = 1,170).

[9]These definitions result in equal durations for both categories: SWR$^+$ (93.0 [65.4] ms) and SWR$^-$ (93.0 [65.4] ms).

[10]SWR$^+$ increased against the bootstrap sample; 95th percentile = 0.42 [Hz]; $p < 0.05$.

[11]SWR$^+$ (3.05 [0.85] SD of baseline, median [IQR]; n = 1,170) vs. SWR$^-$ (2.37 [0.33] SD of baseline, median [IQR]; n = 1,170; $p < 0.001$; Brunner–Munzel test).

[12]1.25 [1.30], median [IQR], n = 1,281 in Match IN task; 1.12 [1.35], median [IQR], n = 1,163 in Mismatch OUT task

[13]1.08 [1.07], median [IQR], n = 1,149 in Match IN task; 0.90 [1.12], median [IQR], n = 1,088 in Mismatch OUT task

[14]1.32 [1.24], median [IQR], n = 935 in Match IN task; 1.15 [1.26], median [IQR], n = 891 in Mismatch OUT task

[15]1.19 [0.96], median [IQR], n = 673 in Match IN task; 0.94 [0.88], median [IQR], n = 664 in Mismatch OUT task

To provide two-dimensional visualization, we linearly aligned peri-SWR NTs by setting g_E at the origin $(0, 0)$ and g_R at $(\|g_E g_R\|, 0)$. Subsequently, we rotated these aligned NTs around the $g_E g_R$ axis (the x axis), ensuring that the distances from the origin O in the original three-dimensional spaces and angles from $\overrightarrow{g_E g_R}$ are retained in the two-dimensional equivalent.

Scatter plot visualization of NTs within these two-dimensional spaces revealed distinct distributions of peri-SWR NTs based on phases and task types. A notable example of this is the observation that the magnitude of $\|\text{mid-eSWR}^+\|$ exceeds that of $\|\text{pre-eSWR}^+\|$ (Figure 6B), which is consistent with our previous observations (Figure 5).

3.7. Fluctuations of Hippocampal NTs between Encoding and Retrieval States

Subsequently, we investigated the 'direction' of the NT in relation to $\overrightarrow{g_E g_R}$, which was found to be dependent on memory load (Figure 3). The directions of the SWRs were determined by the NT at -250 ms and $+250$ ms from their center, denoted as, for example, $\overrightarrow{\text{eSWR}^+}$. We calculated the cosine similarities between $\overrightarrow{g_E g_R}$, $\overrightarrow{\text{eSWR}}$, and $\overrightarrow{\text{rSWR}}$ in both SWR (SWR$^+$) $and baseline periods (SWR^-)$ $(Figure 7A--D)$. $\overrightarrow{\text{rSWR}^-} \cdot \overrightarrow{g_E g_R}$ exhibited a biphasic distribution. By computing the difference between the distribution of $\overrightarrow{\text{rSWR}^+} \cdot \overrightarrow{g_E g_R}$ (Figure 7A & B) and that of $\overrightarrow{\text{rSWR}^-} \cdot \overrightarrow{g_E g_R}$ (Figure 7C & D), we were able to determine the contributions of SWR (Figure 7E & F), which indicated a shift in the direction of $\overrightarrow{g_E g_R}$ (Figure 7E & F: *red rectangles*).

Furthermore, $\overrightarrow{\text{eSWR}^+} \cdot \overrightarrow{\text{rSWR}^+}$ was less than $\overrightarrow{\text{eSWR}^-} \cdot \overrightarrow{\text{rSWR}^-}$ strictly in Mismatch OUT task (Figure 7F: *pink circles*). In other words, eSWR and rSWR pointed in the opposite direction exclusively in Mismatch OUT task but not Match IN task (Figure 7E: *pink circles*).

4. Discussion

This study hypothesizes that in low-dimensional spaces during a WM task in humans, hippocampal neurons form unique NTs, primarily during SWR periods. Initially, multi-unit spikes in the MTL regions were projected onto three-dimensional spaces during a Sternberg task using GPFA (Figure 1D–E & Figure 2A). The NT distances across WM phases ($\|g_F g_E\|$, $\|g_F g_M\|$, $\|g_F g_R\|$,

$\|g_E g_M\|$, $\|g_E g_R\|$, and $\|g_M g_R\|$) were significantly larger in the hippocampus compared to the EC and amygdala (Figure 2C–E), indicating dynamic and responsive neural activity in the hippocampus during the WM task. Also, in the hippocampus, the NT distance between the encoding and retrieval phases ($\|g_F g_E\|$) correlated positively with memory load (Figure 3C–D), reflecting WM processing. The hippocampal neural NT transiently expanded during SWRs (Figure 5). Lastly, the hippocampal neural NT alternated between encoding and retrieval states, transitioning from encoding to retrieval during SWR events (Figure 7). These findings explain aspects of hippocampal neural activity during a WM task in humans and offer new insights into SWRs as a state-switching element in hippocampal neural states.

The distance of the neural NT across the phases was significantly longer in the hippocampus compared to the EC and amygdala, even when considering the distance from O in these regions (Figure 2C–E). This establishes the involvement of the hippocampus in the WM task, corroborating previous studies indicating hippocampal persistent firing during the maintenance phase [3] [4] [5] [6]. However, in the present study, applying GPFA to multi-unit activity during a one-second level resolution of the WM task revealed that the neural NT in low-dimensional space presented a memory-load dependency between the encoding and retrieval phases, denoted as $\|g_E g_R\|$ (Figure 3). These findings support the association of the hippocampus with WM processing.

Our analysis focused on putative CA1 regions (Figure 4), is supported by several factors. This specific focus results from established observations that SWRs synchronize with interneuron and pyramidal neuron spike bursts [45] [46] [47] [48], potentially within a 50 μm radius of the recording site [49]. Furthermore, we identified an increased incidence of SWRs during the first 0–400 ms of the retrieval phase (Figure 4D). This finding aligns with previous reports of heightened SWR occurrence preceding spontaneous verbal recall [21] [22], supporting our results under a triggered retrieval condition. The observed log-normal distributions of both SWR duration and ripple band peak amplitude in this study (Figure 4C & E) coincide with the current consensus in this field [40]. Consequently, our decision to limit recording sites to putative CA1 regions likely contributed to improving the precision, or true positive

rate, of SWR detection. Although, the NT distance increase from O during SWRs (Figure 5) might be artificially inflated towards higher values due to channel selection, this potential bias does not substantially challenge our main findings.

Interestingly, during the retrieval phase, NT directions alternated between encoding and retrieval states during both baseline and SWR periods in a task-dependent manner (Figure 7C & D). Additionally, the balance of this fluctuation transitioned from encoding to retrieval state during SWR events (Figure 7 E & F). These results align with previous studies on the role of SWR in memory retrieval [21] [22]. Our findings suggest that (i) neuronal oscillation between encoding and retrieval states occurs during a WM task and (ii) SWR events serve as indicators of the transition in hippocampal neural states from encoding to retrieval during a WM task.

Moreover, our study noted differences specific to the WM-task type between encoding- and retrieval-SWRs (Figure 7E–F). Notably, opposing movements of encoding-SWR (eSWR) and retrieval-SWR (rSWR) were not observed in Match IN task but were apparent in Mismatch OUT task. Memory engram theory [50] might explain these observations: Match In task presented participants with previously shown letters, while Mismatch OUT task introduced a new letter absent in the encoding phase. This explanation underscores the significant role of SWR in human cognitive processes.

In conclusion, this study illustrates that during a WM task in humans, hippocampal activity fluctuate between encoding and retrieval states, uniquely transitioning from encoding to retrieval during SWR events. These findings offer novel insights into the neural correlates and functionality of working memory within the hippocampus.

References

[1] W. B. Scoville, B. Milner, LOSS OF RECENT MEMORY AFTER BILATERAL HIPPOCAMPAL LESIONS, Journal of Neurology, Neurosurgery, and Psychiatry 20 (1) (1957) 11–21. URL https://www.ncbi.nlm.nih.gov/pmc/articles/PMC497229/

[2] L. R. Squire, The Legacy of Patient H.M. for Neuroscience, Neuron 61 (1) (2009) 6–9. doi:10.1016/j.neuron.2008.12.023. URL https://www.ncbi.nlm.nih.gov/pmc/articles/PMC2649674/

[3] E. Boran, T. Fedele, P. Klaver, P. Hilfiker, L. Stieglitz, T. Grunwald, J. Sarnthein, Persistent hippocampal neural firing and hippocampal-cortical coupling predict verbal working memory load, Science Advances 5 (3) (2019) eaav3687. doi:10.1126/sciadv.aav3687. URL https://www.science.org/doi/10.1126/sciadv.aav3687

[4] J. Kamiński, S. Sullivan, J. M. Chung, I. B. Ross, A. N. Mamelak, U. Rutishauser, Persistently active neurons in human medial frontal and medial temporal lobe support working memory, Nature Neuroscience 20 (4) (2017) 590–601, number: 4 Publisher: Nature Publishing Group. doi:10.1038/nn.4509. URL https://www.nature.com/articles/nn.4509

[5] S. Kornblith, R. Q. Quiroga, C. Koch, I. Fried, F. Mormann, Persistent Single-Neuron Activity during Working Memory in the Human Medial Temporal Lobe, Current Biology 27 (7) (2017) 1026–1032, publisher: Elsevier. doi:10.1016/j.cub.2017.02.013. URL https://www.cell.com/current-biology/abstract/S0960-9822(17)30149-5

[6] M. C. M. Faraut, A. A. Carlson, S. Sullivan, O. Tudusciuc, I. Ross, C. M. Reed, J. M. Chung, A. N. Mamelak, U. Rutishauser, Dataset of human medial temporal lobe single neuron activity during declarative memory encoding and recognition, Scientific Data 5 (1) (2018) 180010, number: 1 Publisher: Nature Publishing Group. doi:10.1038/sdata.2018.10. URL https://www.nature.com/articles/sdata201810

[7] A. A. Borders, C. Ranganath, A. P. Yonelinas, The hippocampus supports high-precision binding in visual working memory, Hippocampus 32 (3) (2022) 217–230. doi:10.1002/hipo.23401.

[8] J. Li, D. Cao, S. Yu, X. Xiao, L. Imbach, L. Stieglitz, J. Sarnthein, T. Jiang, Functional specialization and interaction in the amygdala-hippocampus circuit during working memory processing, Nature Communications 14 (1) (2023) 2921, number: 1 Publisher: Nature Publishing Group. doi:10.1038/s41467-023-38571-w. URL https://www.nature.com/articles/s41467-023-38571-w

[9] V. Dimakopoulos, P. Mégevand, L. H. Stieglitz, L. Imbach, J. Sarnthein, Information flows from hippocampus to auditory cortex during replay of verbal working memory items, eLife 11 (2022) e78677, publisher: eLife Sciences Publications, Ltd. doi:10.7554/eLife.78677. URL https://doi.org/10.7554/eLife.78677

[10] G. Buzsáki, Hippocampal sharp wave-ripple: A cognitive biomarker for episodic memory and planning, Hippocampus 25 (10) (2015) 1073–1188, _eprint: https://onlinelibrary.wiley.com/doi/pdf/10.1002/hipo.22488. doi:https://doi.org/10.1002/hipo.22488. URL https://onlinelibrary.wiley.com/doi/abs/10.1002/hipo.22488

[11] M. A. Wilson, B. L. McNaughton, Reactivation of hippocampal ensemble memories during sleep, Science (New York, N.Y.) 265 (5172) (1994) 676–679. doi:10.1126/science.8036517.

[12] Z. Nádasdy, H. Hirase, A. Czurkó, J. Csicsvari, G. Buzsáki, Replay and Time Compression of Recurring Spike Sequences

in the Hippocampus, Journal of Neuroscience 19 (21) (1999) 9497–9507, publisher: Society for Neuroscience Section: ARTICLE. doi:10.1523/JNEUROSCI.19-21-09497.1999. URL https://www.jneurosci.org/content/19/21/9497

[13] A. K. Lee, M. A. Wilson, Memory of sequential experience in the hippocampus during slow wave sleep, Neuron 36 (6) (2002) 1183–1194. doi:10.1016/s0896-6273(02)01096-6.

[14] K. Diba, G. Buzsáki, Forward and reverse hippocampal place-cell sequences during ripples, Nature Neuroscience 10 (10) (2007) 1241–1242, number: 10 Publisher: Nature Publishing Group. doi:10.1038/nn1961.
URL https://www.nature.com/articles/nn1961

[15] T. J. Davidson, F. Kloosterman, M. A. Wilson, Hippocampal replay of extended experience, Neuron 63 (4) (2009) 497–507. doi:10.1016/j.neuron.2009.07.027.

[16] G. Girardeau, K. Benchenane, S. I. Wiener, G. Buzsáki, M. B. Zugaro, Selective suppression of hippocampal ripples impairs spatial memory, Nature Neuroscience 12 (10) (2009) 1222–1223. doi:10.1038/nn.2384.
URL http://www.nature.com/articles/nn.2384

[17] V. Ego-Stengel, M. A. Wilson, Disruption of ripple-associated hippocampal activity during rest impairs spatial learning in the rat, Hippocampus 20 (1) (2010) 1–10. doi:10.1002/hipo.20707.

[18] A. Fernández-Ruiz, A. Oliva, E. Fermino de Oliveira, F. Rocha-Almeida, D. Tingley, G. Buzsáki, Long-duration hippocampal sharp wave ripples improve memory, Science (New York, N.Y.) 364 (6445) (2019) 1082–1086. doi:10.1126/science.aax0758.
URL https://www.ncbi.nlm.nih.gov/pmc/articles/PMC6693581/

[19] J. Kim, A. Joshi, L. Frank, K. Ganguly, Cortical–hippocampal coupling during manifold exploration in motor cortex, Nature (2022) 1–8Publisher: Nature Publishing Group. doi:10.1038/s41586-022-05533-z.
URL https://www.nature.com/articles/s41586-022-05533-z

[20] C.-T. Wu, D. Haggerty, C. Kemere, D. Ji, Hippocampal awake replay in fear memory retrieval, Nature Neuroscience 20 (4) (2017) 571–580. doi:10.1038/nn.4507.

[21] Y. Norman, E. M. Yeagle, S. Khuvis, M. Harel, A. D. Mehta, R. Malach, Hippocampal sharp-wave ripples linked to visual episodic recollection in humans, Science 365 (6454) (2019) eaax1030. doi:10.1126/science.aax1030.
URL https://www.sciencemag.org/lookup/doi/10.1126/science.aax1030

[22] Y. Norman, O. Raccah, S. Liu, J. Parvizi, R. Malach, Hippocampal ripples and their coordinated dialogue with the default mode network during recent and remote recollection, Neuron 109 (17) (2021) 2767–2780.e5, publisher: Elsevier. doi:10.1016/j.neuron.2021.06.020.
URL https://www.cell.com/neuron/abstract/S0896-6273(21)00461-X

[23] C. J. Behrens, L. P. van den Boom, L. de Hoz, A. Friedman, U. Heinemann, Induction of sharp wave–ripple complexes in vitro and reorganization of hippocampal networks, Nature Neuroscience 8 (11) (2005) 1560–1567, number: 11 Publisher: Nature Publishing Group. doi:10.1038/nn1571.

URL https://www.nature.com/articles/nn1571

[24] H. Norimoto, K. Makino, M. Gao, Y. Shikano, K. Okamoto, T. Ishikawa, T. Sasaki, H. Hioki, S. Fujisawa, Y. Ikegaya, Hippocampal ripples down-regulate synapses, Science (New York, N.Y.) 359 (6383) (2018) 1524–1527. doi:10.1126/science.aao0702.

[25] J. O'Keefe, J. Dostrovsky, The hippocampus as a spatial map: Preliminary evidence from unit activity in the freely-moving rat, Brain Research 34 (1971) 171–175, place: Netherlands Publisher: Elsevier Science. doi:10.1016/0006-8993(71)90358-1.

[26] J. O'Keefe, Place units in the hippocampus of the freely moving rat, Experimental Neurology 51 (1) (1976) 78–109. doi:10.1016/0014-4886(76)90055-8.
URL https://www.sciencedirect.com/science/article/pii/0014488676900558

[27] A. D. Ekstrom, M. J. Kahana, J. B. Caplan, T. A. Fields, E. A. Isham, E. L. Newman, I. Fried, Cellular networks underlying human spatial navigation, Nature 425 (6954) (2003) 184–188, number: 6954 Publisher: Nature Publishing Group. doi:10.1038/nature01964.
URL https://www.nature.com/articles/nature01964

[28] K. B. Kjelstrup, T. Solstad, V. H. Brun, T. Hafting, S. Leutgeb, M. P. Witter, E. I. Moser, M.-B. Moser, Finite Scale of Spatial Representation in the Hippocampus, Science 321 (5885) (2008) 140–143, publisher: American Association for the Advancement of Science. doi:10.1126/science.1157086.
URL https://www.science.org/doi/abs/10.1126/science.1157086

[29] C. D. Harvey, F. Collman, D. A. Dombeck, D. W. Tank, Intracellular dynamics of hippocampal place cells during virtual navigation, Nature 461 (7266) (2009) 941–946, number: 7266 Publisher: Nature Publishing Group. doi:10.1038/nature08499.
URL https://www.nature.com/articles/nature08499

[30] H. Zhang, P. D. Rich, A. K. Lee, T. O. Sharpee, Hippocampal spatial representations exhibit a hyperbolic geometry that expands with experience, Nature Neuroscience (Dec. 2022). doi:10.1038/s41593-022-01212-4.
URL https://www.nature.com/articles/s41593-022-01212-4

[31] P. A. Naber, F. H. Lopes da Silva, M. P. Witter, Reciprocal connections between the entorhinal cortex and hippocampal fields CA1 and the subiculum are in register with the projections from CA1 to the subiculum, Hippocampus 11 (2) (2001) 99–104, _eprint: https://onlinelibrary.wiley.com/doi/pdf/10.1002/hipo.1028. doi:10.1002/hipo.1028.
URL https://onlinelibrary.wiley.com/doi/abs/10.1002/hipo.1028

[32] N. M. van Strien, N. L. M. Cappaert, M. P. Witter, The anatomy of memory: an interactive overview of the parahippocampal–hippocampal network, Nature Reviews Neuroscience 10 (4) (2009) 272–282, number: 4 Publisher: Nature Publishing Group. doi:10.1038/nrn2614.
URL https://www.nature.com/articles/nrn2614

[33] B. A. Strange, M. P. Witter, E. S. Lein, E. I. Moser, Functional organization of the hippocampal longitudinal axis, Nature Reviews Neuroscience 15 (10) (2014) 655–669, number: 10 Pub-

lisher: Nature Publishing Group. `doi:10.1038/nrn3785`. URL `https://www.nature.com/articles/nrn3785`

[34] R. J. Gardner, E. Hermansen, M. Pachitariu, Y. Burak, N. A. Baas, B. A. Dunn, M.-B. Moser, E. I. Moser, Toroidal topology of population activity in grid cells, Nature 602 (7895) (2022) 123–128, number: 7895 Publisher: Nature Publishing Group. `doi:10.1038/s41586-021-04268-7`.
URL `https://www.nature.com/articles/s41586-021-04268-7`

[35] S. P. Jadhav, C. Kemere, P. W. German, L. M. Frank, Awake Hippocampal Sharp-Wave Ripples Support Spatial Memory, Science 336 (6087) (2012) 1454–1458, publisher: American Association for the Advancement of Science. `doi:10.1126/science.1217230`.
URL `https://www.science.org/doi/abs/10.1126/science.1217230`

[36] Y. Watanabe, M. Okada, Y. Ikegaya, Towards threshold invariance in defining hippocampal ripples, Journal of Neural Engineering 18 (6) (2021) 066012. `doi:10.1088/1741-2552/ac3266`.
URL `https://dx.doi.org/10.1088/1741-2552/ac3266`

[37] E. Boran, T. Fedele, A. Steiner, P. Hilfiker, L. Stieglitz, T. Grunwald, J. Sarnthein, Dataset of human medial temporal lobe neurons, scalp and intracranial EEG during a verbal working memory task, Scientific Data 7 (1) (2020) 30, number: 1 Publisher: Nature Publishing Group. `doi:10.1038/s41597-020-0364-3`.
URL `https://www.nature.com/articles/s41597-020-0364-3`

[38] B. M. Yu, J. P. Cunningham, G. Santhanam, S. I. Ryu, K. V. Shenoy, M. Sahani, Gaussian-Process Factor Analysis for Low-Dimensional Single-Trial Analysis of Neural Population Activity, Journal of Neurophysiology 102 (1) (2009) 614–635. `doi:10.1152/jn.90941.2008`.
URL `https://www.ncbi.nlm.nih.gov/pmc/articles/PMC2712272/`

[39] J. Niediek, J. Boström, C. E. Elger, F. Mormann, Reliable Analysis of Single-Unit Recordings from the Human Brain under Noisy Conditions: Tracking Neurons over Hours, PLOS ONE 11 (12) (2016) e0166598, publisher: Public Library of Science. `doi:10.1371/journal.pone.0166598`.
URL `https://journals.plos.org/plosone/article?id=10.1371/journal.pone.0166598`

[40] A. A. Liu, S. Henin, S. Abbaspoor, A. Bragin, E. A. Buffalo, J. S. Farrell, D. J. Foster, L. M. Frank, T. Gedankien, J. Gotman, J. A. Guidera, K. L. Hoffman, J. Jacobs, M. J. Kahana, L. Li, Z. Liao, J. J. Lin, A. Losonczy, R. Malach, M. A. van der Meer, K. McClain, B. L. McNaughton, Y. Norman, A. Navas-Olive, L. M. de la Prida, J. W. Rueckemann, J. J. Sakon, I. Skelin, I. Soltesz, B. P. Staresina, S. A. Weiss, M. A. Wilson, K. A. Zaghloul, M. Zugaro, G. Buzsáki, A consensus statement on detection of hippocampal sharp wave ripples and differentiation from other fast oscillations, Nature Communications 13 (1) (2022) 6000, number: 1 Publisher: Nature Publishing Group. `doi:10.1038/s41467-022-33536-x`.
URL `https://www.nature.com/articles/s41467-022-33536-x`

[41] K. Kay, M. Sosa, J. E. Chung, M. P. Karlsson, M. C. Larkin, L. M. Frank, A hippocampal network for spatial coding during

immobility and sleep, Nature 531 (7593) (2016) 185–190. `doi:10.1038/nature17144`.

[42] L. McInnes, J. Healy, N. Saul, L. Großberger, UMAP: Uniform Manifold Approximation and Projection, Journal of Open Source Software 3 (29) (2018) 861. `doi:10.21105/joss.00861`.
URL `https://joss.theoj.org/papers/10.21105/joss.00861`

[43] P. J. Rousseeuw, Silhouettes: A graphical aid to the interpretation and validation of cluster analysis, Journal of Computational and Applied Mathematics 20 (1987) 53–65. `doi:10.1016/0377-0427(87)90125-7`.
URL `https://www.sciencedirect.com/science/article/pii/0377042787901257`

[44] P. Virtanen, R. Gommers, T. E. Oliphant, M. Haberland, T. Reddy, D. Cournapeau, E. Burovski, P. Peterson, W. Weckesser, J. Bright, S. J. van der Walt, M. Brett, J. Wilson, K. J. Millman, N. Mayorov, A. R. J. Nelson, E. Jones, R. Kern, E. Larson, C. J. Carey, Polat, Y. Feng, E. W. Moore, J. VanderPlas, D. Laxalde, J. Perktold, R. Cimrman, I. Henriksen, E. A. Quintero, C. R. Harris, A. M. Archibald, A. H. Ribeiro, F. Pedregosa, P. van Mulbregt, SciPy 1. 0 Contributors, SciPy 1.0: fundamental algorithms for scientific computing in Python, Nature Methods 17 (2020) 261–272, aDS Bibcode: 2020NatMe..17..261V. `doi:10.1038/s41592-019-0686-2`.
URL `https://ui.adsabs.harvard.edu/abs/2020NatMe..17..261V`

[45] G. Buzsáki, Two-stage model of memory trace formation: a role for "noisy" brain states, Neuroscience 31 (3) (1989) 551–570. `doi:10.1016/0306-4522(89)90423-5`.

[46] M. L. V. Quyen, A. Bragin, R. Staba, B. Crépon, C. L. Wilson, J. Engel, Cell Type-Specific Firing during Ripple Oscillations in the Hippocampal Formation of Humans, Journal of Neuroscience 28 (24) (2008) 6104–6110, publisher: Society for Neuroscience Section: Brief Communications. `doi:10.1523/JNEUROSCI.0437-08.2008`.
URL `https://www.jneurosci.org/content/28/24/6104`

[47] S. Royer, B. V. Zemelman, A. Losonczy, J. Kim, F. Chance, J. C. Magee, G. Buzsáki, Control of timing, rate and bursts of hippocampal place cells by dendritic and somatic inhibition, Nature Neuroscience 15 (5) (2012) 769–775, number: 5 Publisher: Nature Publishing Group. `doi:10.1038/nn.3077`.
URL `https://www.nature.com/articles/nn.3077`

[48] N. Hájos, M. R. Karlócai, B. Németh, I. Ulbert, H. Monyer, G. Szabó, F. Erdélyi, T. F. Freund, A. I. Gulyás, Input-output features of anatomically identified CA3 neurons during hippocampal sharp wave/ripple oscillation in vitro, The Journal of Neuroscience: The Official Journal of the Society for Neuroscience 33 (28) (2013) 11677–11691. `doi:10.1523/JNEUROSCI.5729-12.2013`.

[49] E. W. Schomburg, C. A. Anastassiou, G. Buzsáki, C. Koch, The Spiking Component of Oscillatory Extracellular Potentials in the Rat Hippocampus, The Journal of Neuroscience 32 (34) (2012) 11798–11811. `doi:10.1523/JNEUROSCI.0656-12.2012`.
URL `https://www.ncbi.nlm.nih.gov/pmc/articles/PMC3459239/`

[50] X. Liu, S. Ramirez, P. T. Pang, C. B. Puryear, A. Govindara-

jan, K. Deisseroth, S. Tonegawa, Optogenetic stimulation of a hippocampal engram activates fear memory recall, Nature 484 (7394) (2012) 381–385, number: 7394 Publisher: Nature Publishing Group. `doi:10.1038/nature11028`.
URL `https://www.nature.com/articles/nature11028`

Contributors

Y.W. and T.Y. conceptualized the study; Y.W. performed the data analysis; Y.W. and T.Y. wrote the original draft; and all authors reviewed the final manuscript.

Acknowledgments

Declaration of Interests

The authors declare that they have no competing interests.

Data and code availability

The data is available on G-Node (`https://doi.gin.g-node.org/10.12751/g-node.d76994/`).
The source code is available on GitHub (`https://github.com/yanagisawa-lab/hippocampal-neural-fluctuation-during-a-WM-task-in-humans`).

Inclusion and Diversity Statement

We support inclusive, diverse, and equitable conduct of research.

Declaration of Generative AI in Scientific Writing

The authors employed ChatGPT, provided by OpenAI, for enhancing the manuscript's English language quality. After incorporating the suggested improvements, the authors meticulously revised the content. Ultimate responsibility for the final content of this publication rests entirely with the authors.

Tables

Subject ID	# of sessions	AHL	AHR	PHL	PHR	ECL	ECR	AL	AR	SOZ
1	4	✓	n.a.	✓	✓	✓	n.a.	✓	n.a.	AHR & LR
2	7	✓	✓	✓	✓	✓	✓	✓	✓	AHR & PHR
3	3	✓	✓	✓	✓	✓	✓	✓	n.a.	AHL & PHL
4	2	✓	✓	✓	✓	✓	✓	✓	✓	AHL & AHR & PHL & PHR
5	3	✓	n.a.	n.a.	✓	n.a.	n.a.	✓	n.a.	DRR
6	6	✓	✓	✓	✓	✓	✓	✓	✓	AHL & PHL & ECL & AL
7	4	✓	✓	✓	✓	✓	✓	✓	✓	AHR & PHR
8	5	✓	✓	✓	✓	✓	✓	✓	✓	ECR
9	2	✓	✓	✓	✓	✓	✓	✓	✓	ECR & AR

Table 1 – Electrode Distribution within the Dataset

This figure denotes the placements of electrodes and seizure onset zones. Regions marked with ✓ were included in the dataset, while those imprinted with n.a. were absent. The abbreviations used are as follows: AHL, left hippocampal head; AHR, right hippocampal head; PHL, left hippocampal body; PHR, right hippocampal body; ECL, left entorhinal cortex; ECR, right entorhinal cortex; AL, left amygdala; AR, right amygdala; SOZ represents the seizure onset zone.

Subject	AHL	AHR	PHL	PHR
1	0.60 ± 0.14	n.a.	n.a.	0.1 ± 0
2	0.21 ± 0.16	0.17 ± 0.21	0.18 ± 0.22	0.20 ± 0.15
3	0.40 ± 0.42	0.83 ± 0.12	n.a.	n.a.
4	0.10 ± 0.00	0.10 ± 0.00	0.90 ± 0.00	0.10 ± 0.14
5	n.a.	n.a.	n.a.	n.a.
6	0.63 ± 0.06	n.a.	n.a.	0.27 ± 0.06
7	0.10 ± 0.00	0.35 ± 0.35	0.37 ± 0.47	0.10 ± 0.00
8	0.13 ± 0.10	n.a.	0.28 ± 0.49	n.a.
9	n.a.	0.85 ± 0.07	0.15 ± 0.07	n.a.

Table 2 – Silhouette Score of UMAP Clustering for SWR+ Candidates and SWR- Candidates

The silhouette scores (mean ±SD across sessions per subject) for UMAP clustering of SWR+ candidates and SWR- candidates are based on their respective multi-unit spike patterns (Figure 4A). The mean scores were 0.205 and the standard deviation was 0.285, calculated for the interquartile range (IQR; Figure 4B).

Subject ID	# of sessions	# of trials	ROI	# of SWRs	SWR incidence [Hz]
#1	2	100	AHL	274	0.34
#3	2	97	AHR	325	0.42
#4	2	99	PHL	202	0.26
#6	2	100	AHL	297	0.37
#9	2	97	AHR	72	0.09
	Total = 10	Total = 493		Total = 1170	0.30 ± 0.13 (mean ± SD)

Table 3 – Summary of Detected SWRs

The table provides statistics of presumptive CA1 regions and SWR events. Only the initial two sessions (sessions 1 and 2) from each subject were included in our analysis to reduce sampling bias.

Figures

Figure 1 – Local Field Potentials, Multiunit Activity, and Neural Trajectories in the Hippocampus During a Modified Sternberg Task

A. Representative wideband LFP signals for intracranial EEG recording from the left hippocampal head are presented. This recording took place while the subject performed a modified Sternberg working memory task. Task stages included fixation (1 s, *gray*), encoding (2 s, *blue*), maintenance (3 s, *green*), and retrieval (2 s, *red*). *B.* Displays the associated ripple band LFP traces. Note *purple* and *yellow* rectangles, which denote the timings for SWR⁺ candidates and SWR⁻ candidates, respectively (the latter serving as control events for SWR⁺). *C.* A raster plot illustrates multi-unit spikes from the LFP traces. These spikes have been sorted using a spike algorithm [39]. *D.* Shows neural trajectories (NTs) computed by GPFA[38] based on spike counts per unit with 50-ms bins. The geometric median of each phase is marked by dot circles. *E.* Indicates the distance of the NT from the origin point *O*.
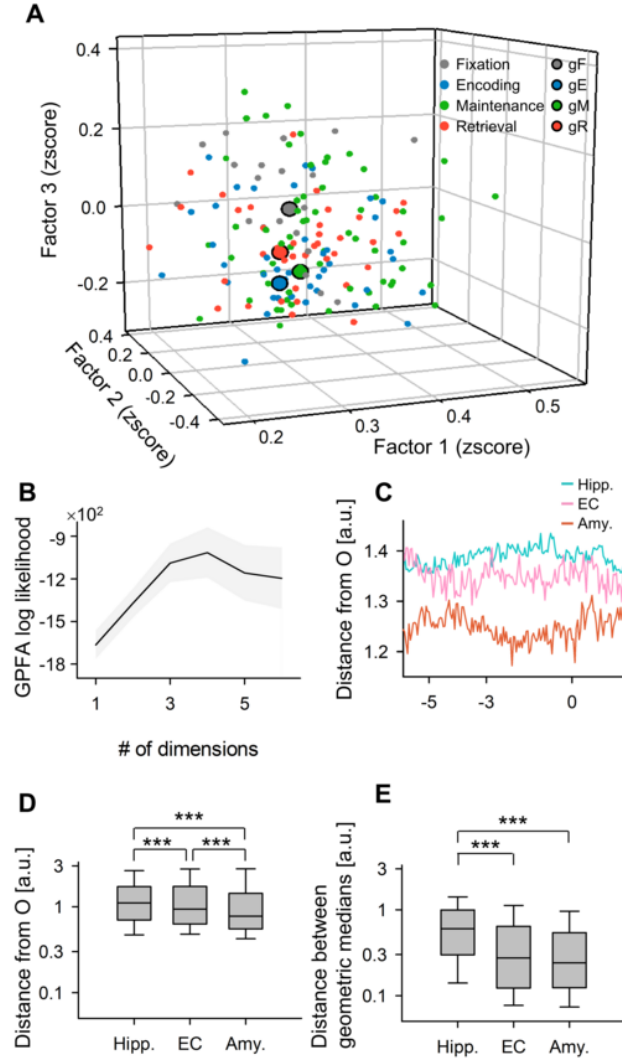
Figure 2 – State-Dependent Neural Trajectory of Hippocampal Neurons

A. Neural trajectories (NTs) depicted as a point cloud within the first three-dimensional factors derived from GPFA [38]. The smaller dots represent 50-ms NT bins, and the larger dots with *black* edges denote the geometric medians for each phase in the Sternberg working memory task: fixation ($\|g_F\|$, *gray*), encoding ($\|g_E\|$, *blue*), maintenance ($\|g_M\|$, *green*), and retrieval ($\|g_R\|$, *red*). *B.* The figure presents the log-likelihood of the GPFA models versus the number of dimensions used to embed multi-unit spikes found in the medial temporal lobe (MTL) regions. Specifically, the elbow method identified three as the optimal dimension. *C.* This panel displays the distance of the NTs from the origin (O) for the hippocampus (Hipp.), entorhinal cortex (EC), and amygdala (Amy.), plotted against the time elapsed from the probe onset. *D.* The NT distance from O within the MTL regions is shown. The hippocampus has the greatest distance, followed by the EC and the Amygdala. *E.* The box plot illustrates inter-phase NT distances within the MTL regions.

16

Figure 3 – Positive Correlation between Memory Load and Neural Trajectory Distance in the Hippocampus between Encoding and Retrieval Phases

A. The relationship between set size (number of letters to be encoded) and accuracy in the working memory task (coefficient $= -0.20$, ***$p < 0.001$). **B.** The correlation between set size and response time (coefficient $= 0.23$, ***$p < 0.001$). **C.** The correlation between set size on the inter-phase distances between the encoding and retrieval phases ($\|g_E g_R\|$) (correlation coefficient $= 0.05$, ***$p < 0.001$). **D.** Experimental observations of correlations between set size and the following parameters: accuracy, response time, $\log_{10} \|g_F g_E\|$, $\log_{10} \|g_F g_M\|$, $\log_{10} \|g_F g_R\|$, $\log_{10} \|g_E g_M\|$, $\log_{10} \|g_E g_R\|$, and $\log_{10} \|g_M g_R\|$ represented by *red* dots. The kernel density plots (*gray*) illustrate the corresponding shuffled surrogate with set size ($n = 1,000$) (***ps < 0.001$).

17

Figure 4 – Detection of SWRs in Putative CA1 Regions

A. Two-dimensional UMAP [42] projection displays multi-unit spikes during SWR⁺ candidates (*purple*) and SWR⁻ candidates (*yellow*). **B.** A cumulative density plot indicates silhouette scores, reflecting UMAP clustering quality (see Table 2). Hippocampal regions with silhouette scores exceeding 0.60 (equivalent to the 75th percentile) are identified as putative CA1 regions. SWR⁺ and SWR⁻ candidates, which were recorded from these regions, are classified as SWR⁺ and SWR⁻ respectively (*n*s = 1,170). **C.** Identical distributions of durations are presented for SWR⁺ (*purple*) and SWR⁻ (*yellow*), based on their definitions (93.0 [65.4] ms, median [IQR]). **D.** SWR incidence for both SWR⁺ (*purple*) and SWR⁻ (*yellow*), relative to the probe's timing, is illustrated as a mean ±95% confidence interval. However, intervals may not be visibly apparent due to their confined ranges, be aware that a significant SWR incidence increase was detected during the initial 400 ms of the retrieval phase (0.421 [Hz], *$p < 0.05$, bootstrap test). **E.** Distributions of ripple band peak amplitudes for SWR⁻ (*yellow*; 2.37 [0.33] SD of baseline, median [IQR]) and SWR⁺ (*purple*; 3.05 [0.85] SD of baseline, median [IQR]) are manifested (***$p < 0.001$, the Brunner–Munzel test).
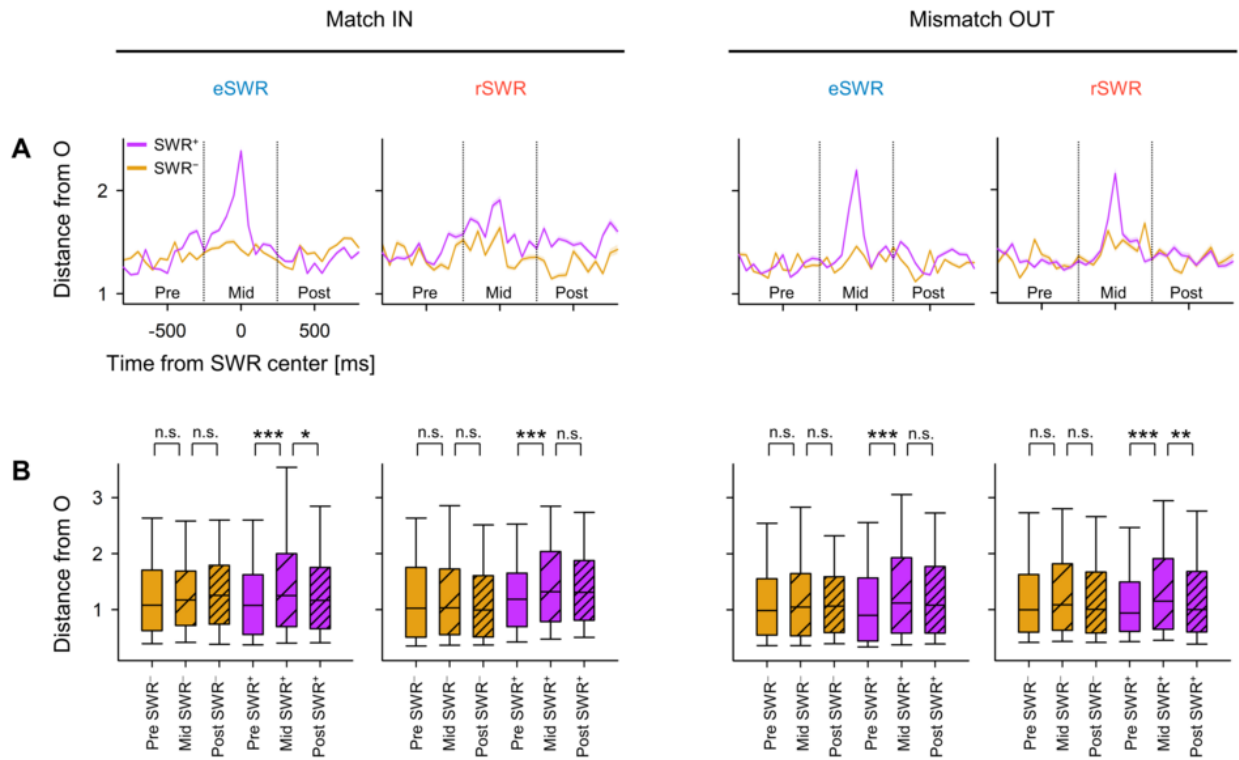
18

Figure 5 – Transient Change in Neural Trajectory during SWR

A. The distance from origin (*O*) of the peri-sharp-wave-ripple neural trajectory (mean ±95% confidence interval). The intervals may be obscured due to their minimal ranges. *B.* The distance from the origin (*O*) during the pre-, mid-, and post-SWR periods is demonstrated (*$p < 0.05$, **$p < 0.01$, ***$p < 0.001$; Brunner–Munzel test applied). Abbreviations: SWR, sharp-wave ripple events; eSWR, SWR during the encoding phase; rSWR, SWR within the retrieval phase; SWR$^+$, positive SWR event; SWR$^-$, control events for SWR$^+$; pre-, mid-, or post-SWR refer to the time intervals from −800 to −250 ms, from −250 to +250 ms, or from +250 to +800 ms, respectively, all relative to the SWR center.

Figure 6 – Visualization of Neural Trajectory During SWR in Two-Dimensional Space

The panels depict hippocampal neural trajectories (NTs) during SWR projected onto two-dimensional spaces. ***A.*** Shows the hippocampal NTs as point clouds during pre-SWR⁻ (*gray*), mid-SWR⁻ (*yellow*), and post-SWR⁻ (*black*). ***B.*** Conveys the equivalent for SWR⁺ rather than SWR⁻. The projection was executed as follows: First, a linear transformation placed g_E at the origin O (0,0), and g_R at ($\|g_E g_R\|$, 0). The point cloud was subsequently rotated around the $g_E g_R$ axis (similar to the x axis) for adaptation to two-dimensional spaces. Thus, within these two-dimensional spaces, the distances from point O and the angles for the $g_E g_R$ axis are retained as in the original three-dimensional spaces created by GPFA. Abbreviations: SWR denotes sharp-wave ripple events; eSWR refers to SWR during the encoding phase; rSWR signals SWR during the retrieval phase; SWR⁺, characterizes an SWR event; SWR⁻ signifies control events for SWR⁺; pre-SWR, mid-SWR, or post-SWR, represent the time intervals from −800 to −250 ms, from −250 to +250 ms, or from +250 to +800 ms from the center of the SWR.
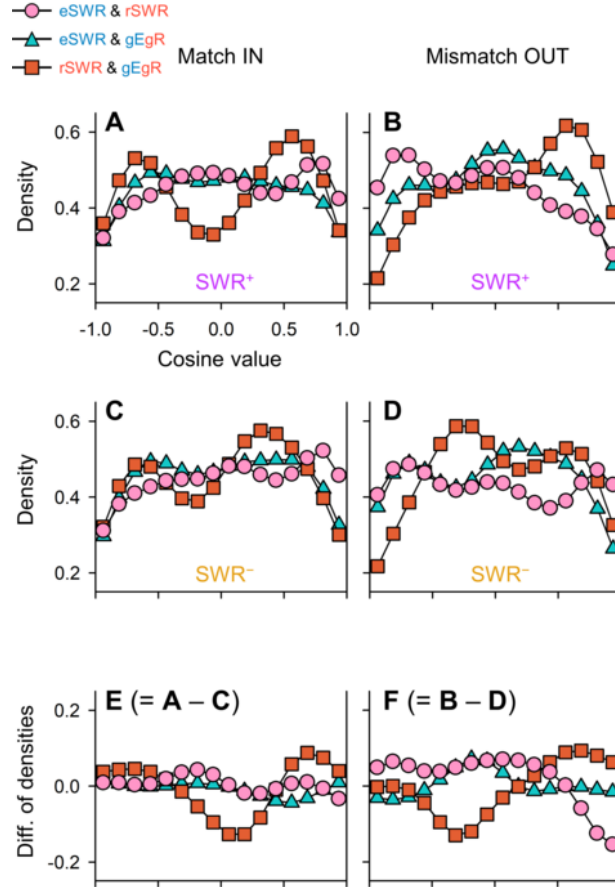
Figure 7 – Direction of Neural Trajectory During SWR Based on Encoding and Retrieval States

A–B The kernel density estimation distributions of $\overrightarrow{eSWR^+} \cdot \overrightarrow{rSWR^+}$ (depicted as pink circles), $\overrightarrow{eSWR^+} \cdot \overrightarrow{g_E g_R}$ (blue triangles), and $\overrightarrow{rSWR^+} \cdot \overrightarrow{g_E g_R}$ (*red rectangles*) in the Match In (*A*) and Mismatch OUT tasks (*B*). *C–D* Illustrates the corresponding distributions of SWR⁻ instead of those of SWR⁺ in *A* and *B*. *E–F* The differences in the distributions of SWR⁺ and SWR⁻, detailing the SWR components (*E = C - A F = D - B*). The biphasic distributions of $\overrightarrow{rSWR^-} \cdot \overrightarrow{g_E g_R}$ indicates fluctuations between the encoding and retrieval states during the Sternberg task. Also, contradicting directionality between $\overrightarrow{eSWR^+}$ and $\overrightarrow{rSWR^+}$ was observed (pink circles) not in Match IN task (*E*), but in Mismatch OUT task (*F*). Lastly, transition from the retrieval to encoding states are apparent in the SWR components in both Match IN and Mismatch OUT tasks (red rectangles in *E–F*).